Crystalchemistry and Oxide Ion Conductivity in the Lanthanum Oxygermanate Apatite Series

L. León-Reina,[†] M. C. Martín-Sedeño,[†] E. R. Losilla,[†] A. Cabeza,[†] M. Martínez-Lara,[†] S. Bruque,[†] F. M. B. Marques,[‡] D. V. Sheptyakov,[§] and M. A. G. Aranda*,[†]

Departamento de Química Inorgánica, Cristalografía y Mineralogía, Universidad de Málaga, 29071 Málaga, Spain, Department of Ceramics and Glass Engineering, CICECO, University of Aveiro, 3810-193 Aveiro, Portugal, and Laboratory for Neutron Scattering, ETHZ & PSI, CH-5232 Villigen PSI, Switzerland

Received January 15, 2003. Revised Manuscript Received March 18, 2003

The $La_{10-x}(GeO_4)_6O_{3-1.5x}$ ($9.33 \leq 10 - x \leq 10$) apatite series has been synthesized and single phases have been obtained in a narrow compositional range ($9.52 \leq 10 - x \leq 9.75$). The apatites' phases are hexagonal (space group (s.g.) $P6_3/m$) for $9.52 \leq 10 - x \leq 9.60$ and triclinic (s.g. $P\bar{1}$) for $9.66 \leq 10 - x \leq 9.75$. The room-temperature crystal structures have been determined from joint Rietveld refinements of neutron and synchrotron X-ray powder diffraction data. $La_{9.60}(GeO_4)_6O_{2.40}$ is hexagonal ($a = 9.9374(1)$ Å, $c = 7.2835(1)$ Å and $V = 622.90(2)$ Å^3) and the Rietveld disagreement factors were low. $La_{9.75}(GeO_4)_6O_{2.62}$ is triclinic ($a = 9.9368(4)$ Å, $b = 9.9220(3)$ Å, $c = 7.2925(2)$ Å, $\alpha = 90.566(3)°$, $\beta = 88.992(4)°$, $\gamma = 120.334(3)°$, and $V = 620.46(3)$ Å^3) and the fits were satisfactory for such complex pseudohexagonal structure. This structure contains 72 variable positional parameters and 24 thermal factors. High-temperature neutron powder diffraction (NPD) data were also collected at 773 and 1173 K for hexagonal $La_{9.60}(GeO_4)_6O_{2.40}$. The electrical results suggest that the samples are bulk oxide ion conductors. The plots of the imaginary parts of the impedance, Z″, and the electric modulus, M″, vs log(frequency), possess maxima for both curves separated by less than a half decade in frequency with associated capacities of ≈2 pF. The curvatures observed in the Arrhenius plots are not due to a phase transition. The conductivities are almost independent of the oxygen partial pressure under oxidizing conditions, which suggests pure oxide-ion conduction with negligible electronic contribution.

Introduction

Apatites form a large family of isostructural compounds with the general formula $A_{10}(TO_4)_6X_2$ where generally A is a large divalent cation (Ca^{2+}, Sr^{2+}, Pb^{2+}, Cd^{2+}, etc.), TO_4 is a trivalent anionic group (PO_4^{3-}, VO_4^{3-}, AsO_4^{3-}, etc.), and X is a monovalent anion (F^-, OH^-, etc.). The archetypal member of this family is fluoroapatite, $Ca_{10}(PO_4)_6F_2$, which crystallizes in the s.g. $P6_3/m$ with $a = 9.363$ Å and $c = 6.878$ Å.[1] The apatite structure is well-known and its framework is built up of isolated TO_4^{3-} tetrahedra with the large A^{2+} cations located in two sites, one 7-coordinated and another 9-coordinated. This polyhedral network generates channels that run parallel to the *c*-axis where the X^- anions are located, see Figure 1. The apatite structure is highly tolerant to cation and anion substitution; for example, it is possible to substitute divalent calcium for a trivalent cation, if the charge is balanced by substitution of the trivalent phosphate group for a tetravalent group.[2−4] Complete series of fluoro- and oxyapatite were prepared by the substitution pair (La^{3+}, SiO_4^{4-}) for (Ca^{2+}, PO_4^{3-}). Many other related compounds can be

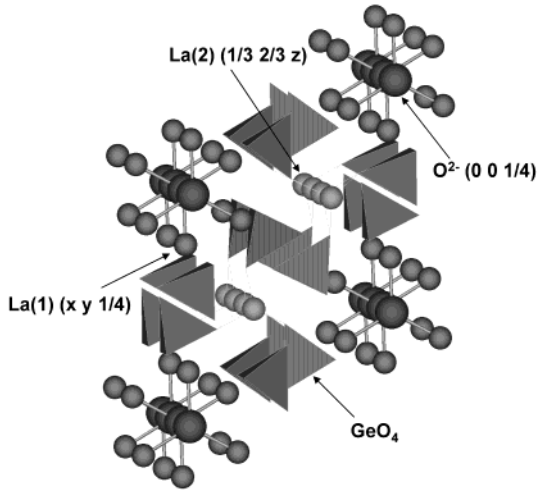

Figure 1. Crystal structure of "ideally stoichiometric $La_{10}(GeO_4)_6O_2$" viewed along the tilted *c*-axis. The different atoms and GeO_4 tetrahedra are labeled.

* To whom correspondence should be addressed via e-mail: g_aranda@uma.es.
[†] Universidad de Málaga.
[‡] University of Aveiro.
[§] Laboratory for Neutron Scattering, ETHZ & PSI.

(1) Sudarsanan, K.; Mackie, P. E.; Young, R. A. *Mater. Res. Bull.* **1972**, *7*, 1331.
(2) Ito, J. *Am. Miner.* **1968**, *53*, 890.
(3) Piriou, B.; Fahmid, D.; Dexpert, A.; Taitai, A.; Lacout, J. *Luminiscence* **1987**, *39*, 97.
(4) Lacout, J. L.; Mikou, M. *Am. Chim.* **1989**, *14*, 9.

10.1021/cm031017u CCC: $25.00
Published on Web 04/16/2003

synthesized, and the crystal structure of oxyapatite, $Ca_{10}(PO_4)_6O$,[5] is known.

Besides the biological importance of apatites, many of these compounds have good luminescent properties[6] and they are also of interest in nuclear waste management.[7] Apatites have cation ion conductivity for appropriate compositions, for instance, $Pb_6Ca_2Li_2(PO_4)_6$.[8] Furthermore, rare-earth (RE)-based apatites have recently attracted considerable attention because of their high oxide ion conductivity.[9] They present conductivities comparable to, or better than, yttria-stabilized zirconia (YSZ) at 873 K. The high oxide ion transference numbers (>0.9) over a wide oxygen partial pressure range, $1-10^{-21}$ atm, and the low activation energy (0.6−0.8 eV) associated with the oxide ion conduction, make them potentially useful as electrolytes for intermediate-temperature solid oxide fuel cells. Most of this initial work on apatite oxides ion conductors has been focused on the Si and Ge derivatives. We can distinguish two related limiting stoichiometries: $RE_{10}(SiO_4)_6O_3$[9−11] and $RE_{9.33}(SiO_4)_6O_2$,[11−17] with the same framework, shown in Figure 1. Atomic substitutions at the A site (for instance La by Sr)[11,18] and at the T site[19,20] are also known. The stoichiometries with Ge are $RE_{10}(GeO_4)_6O_3$[21] and $RE_{9.33}(GeO_4)_6O_2$,[22−24] and cationic substitution at the A site has also been reported.[21,25] There are other related papers describing other oxyapatites containing rare earth cations.[26−28]

Two very important contributions to the knowledge of the relationship between structure and oxide conductivity in the apatite-type compounds are the works of Sansom et al.[12] and Berastegui et al.[23] They used neutron powder diffraction to refine the crystal structures of $La_{9.33}Si_6O_{26}$ and $La_8Sr_2Si_6O_{26}$[12] and $La_{9.33}Ge_6O_{26}$.[23] Sansom et al.[12] suggested that the higher conductivity and lower activation energy for oxide ion conduction in $La_{9.33}Si_6O_{26}$ compared to that of $La_8Sr_2Si_6O_{26}$ are due to the fact that a significant concentration of oxygen ions (∼14%) are displaced from the ideal channel site into new disordered positions in the apatite channels; therefore, high oxide ion conductivity occurs along the channels, and it is enhanced by the atomic disorder.

On the other hand, the $La_2O_3-GeO_2$ pseudo-binary system contains several possible structures and stoichiometries. A very stable compound with a low La/Ge ratio of 1/1 is lanthanum trigermanate germanate, $La_2Ge_2O_7$, the structure of which is known.[29] Another stable compound with higher La/Ge ratio 2/1 is lanthanum oxygermanate, La_2GeO_5, (it is usually formulated as $La_{12}(GeO_4)_6O_6$) whose structure is also known.[23,30] The germanium-containing apatites[21−23] are lanthanum-deficient and they have intermediate La/Ge ratios ranging between 1.66/1 and 1.55/1. For these La/Ge ratios, the apatite structure is obtained if the compounds are prepared at temperatures below 1573 K. Some works[30] erroneously report that syntheses at higher temperatures lead to compounds with lanthanum-deficient La_2GeO_5-type structures maintaining the nominal stoichiometries. Some authors have recently cast doubts on these results.[22,23] We will show that, upon prolonged heating at high temperature, the hexagonal apatite $La_2O_3-GeO_2$ compositions change to lower symmetry. This is due to germanium volatilization and consequent increase of the La/Ge ratio. Very long heating of these apatite compositions (both high and low symmetries) lead to La_2GeO_5 formation due to further germanium loss.[22]

We have centered our study on understanding the relationship between the oxide conductivity and the crystal structures in the $La_{10-x}(GeO_4)_6O_{3-1.5x}$ apatite series. The combined use of powder diffraction (Rietveld method with neutron and synchrotron X-ray data) and impedance spectroscopy has allowed a better understanding of the crystalchemistry and oxide conductivity in this series.

Experimental Section

The series $La_{10-x}(GeO_4)_6O_{3-1.5x}$ ($10 - x = 10.0$, 9.90, 9.80, 9.75, 9.66, 9.60, 9.55, 9.50, and 9.33) was prepared by the ceramic method using high purity oxides: La_2O_3 (Alfa, 99.999%) and GeO_2 (Aldrich, 99.998%). Lanthanum oxide was precalcined at 1273 K for 2 h to achieve decarbonation. The precursors were mixed to prepare 5−8 g of sample by the following overall reaction:

$$(10 - x)/2La_2O_3 + 6GeO_2 \xrightarrow{\Delta} La_{10-x}(GeO_4)_6O_{3-1.5x}$$

The starting mixtures were ground in an agate mortar for 15 min, pelletized, and heated at 1523 K for 6 h in Pt crucibles. After cooling, the samples were ground for 3 h in a Fritsch ball mill (model Pulverizette 7, agate balls and container) at

(5) Henning, P. A.; Landa-Canovas, A. R.; Larsson, A. K.; Lindin, S. *Acta Crystallogr.* **1999**, *B55*, 170.
(6) Davis, T. S.; Kreider E. R.; Parodi, J. A.; Soules, T. F. *J. Lumin.* **1971**, *4*, 48.
(7) McConnell, D. *Apatite*; Springer-Verlag: New York, 1973.
(8) Naddari, T.; Savariault, J. M.; El Feki, H.; Salles, P.; Ben Salah, A. *J. Solid State Chem.* **2002**, *166*, 237−244 (and references therein).
(9) Nakayama, S.; Kageyama, T.; Aono, H.; Sadaoka, Y. *J. Mater. Chem.* **1995**, *5*, 1801
(10) Nakayama, S.; Sakamoto M. *J. Eur. Ceram. Soc.* **1998**, *18*, 1413.
(11) Tao, S.; Irvine, J. T. S. *Mater. Res. Bull.* **2001**, *36*, 1245.
(12) Sansom, J. E. H.; Richings, D.; Slater, P. R. *Solid State Ionics* **2001**, *139*, 205.
(13) Higuchi, M.; Katase, H.; Kodaira, K.; Nakayama, S. *J. Crystal Growth* **2000**, *218*, 282.
(14) Nakayama, S.; Sakamoto, M.; Higuchi, M.; Kodaira, K.; Sato, M.; Kakita, S.; Suzuki, T.; Itoh, K. *J. Eur. Ceram. Soc.* **1999**, *19*, 507.
(15) Higuchi, M.; Kodaira, K.; Nakayama, S. *J. Crystal Growth* **1999**, *207*, 298.
(16) Higuchi, M.; Kodaira, K.; Nakayama, S. *J. Crystal Growth* **2000**, *216*, 317.
(17) Kolitsch, U.; Seifert, H. J.; Aldinger, F.; *J. Solid State Chem.* **1995**, *120*, 38.
(18) Abram, E. J.; Sinclair, D. C.; West, A. R. *J. Mater. Chem.* **2001**, *11*, 1978.
(19) Boyer, L.; Carpena, J.; Lacout, J. L. *Solid State Ionics* **1997**, *95*, 121.
(20) McFarlane, J.; Barth, S.; Swaffer, M.; Sansom, J. E. H.; Slater, P. R. *Ionics* **2002**, *8*, 149.
(21) Arikawa, H.; Nishiguchi, H.; Ishihara T.; Takita Y. *Solid State Ionics* **2000**, *136*, 31.
(22) Sansom, L.; Hildebrandt L.; Slater, P. R. *Ionics* **2002**, *8*, 155.
(23) Berastegui, P.; Hull, S.; García, F. J.; Grins, J. *J. Solid State Chem.* **2002**, *168*, 294.
(24) Nakayama, S.; Sakamoto, M. *J. Mater. Sci. Lett.* **2001**, *20*, 1627.
(25) Takahashi, K.; Uematsu, Z. G.; Sato, M. *J. Solid State Chem.* **1998**, *139*, 304.
(26) Mazza, D.; Ronchetti, S. *Mater. Res. Bull.* **1999**, *34*, 1375.
(27) Bouhaouss, A.; Laghzizil, A.; Bensaoud, A.; Ferhat, M.; Lorent, G.; Livage, J. *Int. J. Inorg. Mater.* **2001**, *3*, 743.
(28) Sato, M.; Kono, Y.; Ueda, H.; Uematsu, A.; Toda, K. *Solid State Ionics* **1996**, *83*, 249.
(29) Smolin, Y. I.; Shepelev, Y. F.; Upatova, T. V. *Doklady Akademii Nauk* **1969**, *187*, 322.
(30) (a)Ishihara, T.; Arikawa, H.; Akbay, T.; Nishiguchi, H.; Takita, Y. *J. Am. Chem. Soc.* **2001**, *123*, 203. (b) Ishihara, T.; Arikawa, H.; Nishiguchi, H.; Takita, Y. *Solid State Ionics* **2002**, *154−155*, 455.

100 rpm with reversed rotation each 20 min. The resulting powders were pelletized again and a second thermal treatment was carried out at 1523 K for 12 h. Weight losses, linked to Ge volatilization, at these temperatures and times were found to be negligible. Ge loss at temperatures higher than 1623 K is indeed a problem.[22] Nine $La_{10-x}(GeO_4)_6O_{3-1.5x}$ samples were prepared which hereafter are labeled as La_{10-x}.

Powder Diffraction. All samples were characterized by laboratory X-ray powder diffraction (LXRPD) at room temperature. The powder patterns were collected on a Siemens D5000 automated diffractometer using graphite-monochromated Cu $K\alpha_{1,2}$ radiation. The compounds were loaded in an aluminum holder and scanned between 15 and 110° (2θ) in 0.03° steps, counting 18 s per step. Thermodiffractometric data were recorded with the same diffractometer but in a second goniometer permanently equipped with a HTK10 heating chamber. The patterns were collected between 298 and 1273 K under He flow over the 19−33° angular range (2θ), with a step size of 0.03°, and counting for 25 s per step. A delay time of 10 min was selected to ensure thermal equilibration of the samples before any pattern was collected. Full structural characterization was carried out for $La_{9.60}$ and $La_{9.75}$ samples by a combined analysis of high-resolution synchrotron X-ray powder diffraction (SXRPD) and neutron powder diffraction (NPD) data.

High-resolution SXRPD patterns were collected on the ID31 diffractometer [European Synchrotron Radiation Facility (ESRF), Grenoble, France] for $La_{9.60}$, $La_{9.66}$, and $La_{9.75}$ materials. The samples were loaded in a borosilicate glass capillary (ϕ = 1.5 mm) and rotated during data collection. A short penetrating wavelength, λ = 0.400269 Å (30.97 keV), was selected with a double-crystal Si (111) monochromator and calibrated with Si standard sample from NIST (a = 5.43094 Å). The overall measuring time was ≈1 h to have very good statistics over the angular range 2−30° (in 2θ) [11.5−0.77 Å]. The data from the multi-analyzer Si(111) stage coupled with the nine scintillation detectors were normalized and summed up to 0.003° step size with local software to produce the final raw data.

Room-temperature NPD patterns were collected on a HRPT diffractometer[31] [SINQ neutron source at Paul Scherrer Institut, Villigen, Switzerland] for $La_{9.60}$ and $La_{9.75}$ materials. The samples were loaded in a vanadium can. High-temperature NPD data were also collected for $La_{9.60}$ at 773 and 1173 K with the sample loaded in a steel can. HRPT was used in the "medium-resolution" mode with a wavelength of ∼1.886 Å which was selected by the (511) reflection of the vertically focusing Ge monochromator. The overall measuring time was ≈10 h per pattern to have good statistics over the 2θ angular range of 5−165° [21−0.95 Å] with 0.05° step size. RT structural data have been obtained from the joint SXRPD and NPD Rietveld refinements[32] by using the GSAS suite of programs.[33]

Differential Thermal Analysis. Data were recorded for all compositions on a Setaram Labsys apparatus. The temperature was varied from RT up to 1573 K at a heating rate of 10 $K \cdot min^{-1}$ with calcined Al_2O_3 as reference.

Impedance. Data were collected on cylindrical pellets (∼10 mm diameter and ∼1 mm thickness) obtained by pressing the fine powder at 400 MPa for 2 min. The pellets were sintered at 1573 K for 6 h to increase the mechanical strength. The pellets were not fully dense and the compactions ranged between 63 and 67% of the theoretical value taking into account the pellets' masses and volumes (and the crystallographic density). No weight losses were detected in this sintering step, which was followed by weighing the pellets before and after the thermal treatment.

Electrodes were made by coating opposite pellet faces with Engelhard platinum paste and gradually heating them to 1073 K in air to decompose the paste and harden the Pt residue. The impedance data were collected using a Hewlett-Packard 4284A impedance analyzer over the frequency range 20 Hz to 1 MHz from 423 to 1273 K. For low-temperature measurements (between 423 and 573 K at 15-K intervals), the pellets were mounted in a Novocontrol Quatro Cryosystem jig. The stabilization time before each data acquisition was 40 min where the maximum temperature variation was 0.1 K. Measurement processes were controlled electronically by the WinDETA package of programs.[34] For the high-temperature measurements (between 573 and 1273 K), the pellets were mounted in a homemade alumina conductivity jig, with the two Pt wires shielded in two alumina tubes, which were placed in a tube furnace. Electrical data were taken every 100 K below 873 K and every 50 K above 873 K. A delay time of 45 min at each temperature was selected to ensure thermal equilibrium. Temperatures were accurate to ±1 K. Finally, long-term conductivity stability was measured every 4 h at 1073 K.

High-temperature measurements as a function of oxygen partial pressure (P_{O_2} range from air to around 10^{-21} atm for N_2-H_2 gas mixtures) were performed in a gas flow cell. The oxygen partial pressure was monitored by using a YSZ oxygen sensor placed next to the pellet in the sample holder. Sample conductivity was continually recorded as a function of P_{O_2}. The process involved flushing the system with N_2 [minimum P_{O_2} was $\approx 10^{-5}$ atm] or N_2-H_2 (10%) gas mixture [minimum P_{O_2} was $\approx 10^{-21}$ atm]. The N_2 and N_2-H_2 gases were used to provide low oxygen activities inside the furnace. After reaching a minimum, the P_{O_2} level was slowly raised back to atmospheric pressure. Each redox cycle took over 10 h to complete. Details of the experimental setup and overall procedure can be found elsewhere.[35,36]

Results and Discussion

Synthesis and Single Phase Existence. The $La_{10-x}(GeO_4)_6O_{3-1.5x}$ ($10 - x$ = 10.0, 9.90, 9.80, 9.75, 9.66, 9.60, 9.55, 9.50, and 9.33) series has been prepared as crystalline phases. The dominant phase in our synthetic conditions was invariably the apatite-type structure. However, some compositions were not single phase. LXRPD patterns for $La_{9.50}$ and $La_{9.33}$ compounds indicated the presence of triclinic $La_2Ge_2O_7$ as minor impurity phase. The analysis of the LXRPD data by the Rietveld method showed that the $La_{9.50}$ and $La_{9.33}$ samples contained 1.5(1)% and 4.9(2)% (w/w) of $La_2Ge_2O_7$, respectively. So, from these data we can establish the lower limit for the existence of the series quite close to $10 - x = 9.52$. LXRPD data for the $La_{9.55}$ and $La_{9.60}$ samples indicated single phase with hexagonal apatite structures. LXRPD data for $La_{9.66}$ and $La_{9.75}$ samples indicated highly distorted apatite-like patterns (with many split peaks) but there was no evidence of another phase, which was confirmed in the high-resolution SXRPD study. LXRPD patterns for $La_{9.80}$, $La_{9.90}$, and La_{10} indicated the presence of monoclinic $La_{12}(GeO_4)_6O_6$ as impurity phase. Hence, the single-phase existence range for the $La_{10-x}(GeO_4)_6O_{3-1.5x}$ series is $9.52 \leq 10 - x \leq 9.75$.

At this point, it seems necessary to discuss the nonstoichiometry range that can be tolerated in apatites. There are several reports describing the properties

(31) Fischer, P.; Frey, G.; Koch, M.; Konnecke, M.; Pomjakushin, V.; Schefer, J.; Thut, R.; Schlumpf, N.; Burge, R.; Greuter, U.; Bondt, S.; Berruyer, E. *Physica B* **2000**, *276−278*, 146.
(32) Rietveld, H. M. *J. Appl. Crystallogr.* **1969**, *2*, 65.
(33) Larson, A. C.; von Dreele, R. B. *GSAS program*; Los Alamos National Lab. Rep. No. LA-UR-86748; 1994.
(34) Novocontrol GmbH. *WinDETA Owner's Manual*; Hundsangen, Germany, 1995.
(35) Navarro, L. M.; Marques F. M. B.; Frade, J. R. *J. Electrochem. Soc.* **1997**, *144*, 267.
(36) Baker, R. T.; Gharbage, B.; Marques, F. M. B. *J. Electrochem. Soc.* **1997**, *144*, 3130.

of $RE^{III}_{10}(T^{IV}O_4)_6O_3$ compounds with the apatite structure.[9−11,21] However, these formulas are only approximations, as such compositions are crystallochemically impossible for apatites. Taking into account that the *c*-axis for this structure is close to 7.3 Å and that the oxide anions are located in the cylindrical channels along this axis (Figure 1), we can estimate the maximum amount of oxide anions that can be accommodated by this network. The approximate average ionic diameter for the oxide anion is (1.4 × 2) 2.8 Å. So, a close disordered packing of oxide spheres along the cylindrical channels yields a maximum content of 2.60 oxide anions per chemical formula. Translated to the reported series, the maximum lanthanum content is $La_{9.73}(GeO_4)_6O_{2.60}$. Stoichiometries with higher La/Ge ratio yield $La_{12}(GeO_4)_6O_6$ as second phase. On the other hand, it is impossible to decrease the La/Ge ratio much lower because the coordination of the germanate tetrahedral groups is no longer satisfied. So, the compromise between the maximum amount of oxide anions that can be accommodated and the problems in the germanate coordinations yields the apatite phase existence limits of $9.52 \leq 10 - x \leq 9.75$.

Room-Temperature Crystal Structures. We have carried out a high-resolution SXRPD study for $La_{9.60}$, $La_{9.66}$, and $La_{9.75}$ compounds because of the strong overlapping in the split peaks of the LXRPD patterns. The synchrotron pattern for $La_{9.60}$ showed anisotropic broadening with asymmetric tails for some reflections. This is very likely linked to the incommensurate diffuse spots recently observed for $La_{9.33}$ by electron diffraction.[23] To properly fit the highly anisotropic SXRPD peaks, the phenomenological multidimensional distribution of lattice metrics approach developed by Rodriguez-Carvajal[37] and later generalized by Stephens[38] has been used (available as function 4 in GSAS). All peaks in the high-resolution SXRPD pattern were accounted for in s.g. $P6_3/m$. The room-temperature unit cell data are given in Table 1.

Many split peaks appeared in the SXRPD patterns for $La_{9.66}$ and $La_{9.75}$ compositions that could not be explained with the hexagonal symmetry (see insets of Figures 2 and 3). However, the pattern appeared to be apatite-type. The distortion steadily increases with the lanthanum content (inset of Figure 2). So, we lowered the symmetry to monoclinic $P2_1/m$ (a maximal nonisomorphic subgroup) by adapting the high-symmetry atomic coordinates to this new space group. Unfortunately, some remaining peaks could not be fitted with the excellent resolution of the synchrotron data. So, we lowered the symmetry further from $P2_1/m$ to triclinic $P\bar{1}$ (subgroup). We could satisfactorily fit the SXRPD patterns for $La_{9.66}$ and $La_{9.75}$ compositions, and the room-temperature unit cell data are given in Table 2. The unit cell volume contracts as lanthanum content increases: 622.9, 621.6, and 620.5Å^3 for $La_{9.60}$, $La_{9.66}$, and $La_{9.75}$, respectively. This densification is clearly due to the filling of the empty positions in the cation-deficient apatite structure. However, these very complex triclinic fits (pseudohexagonal) gave very poor atomic positions for the oxygen atoms as 72 positional parameters have to be refined. So, the crystal structure for $La_{9.66}$ from SXRPD data is not reported.

Table 1. Refined Structural Parameters for $La_{9.60}Ge_6O_{26.4}$ at Different Temperatures

	RT[a]	773 K[b]	1173 K[b]
a/Å	9.9374(1)	9.9634(2)	10.0074(2)
c/Å	7.2835(1)	7.3101(2)	7.3334(2)
V/Å^3	622.90(2)	628.44(4)	636.03(3)
$R_{wp}{}^S/R_{wp}{}^N$/%	9.63/3.54	−/4.02	−/3.18
$R_p{}^S/R_p{}^N$/%	8.16/2.80	−/3.04	−/2.49
$R_F{}^S/R_F{}^N$/%	4.03/2.83	−/5.09	−/4.68
La(1), 6h (x, y, $^1/_4$)			
x	0.2331(1)	0.2290(2)	0.2287(2)
y	−0.0101(1)	−0.0124(2)	−0.0102(3)
Uiso × 100/Å^2	0.89	2.55	3.21
La(2), 4f ($^1/_3$, $^2/_3$, z)[c]			
z	−0.0003(2)	0.0029(5)	0.0011(5)
Uiso × 100/Å^2	1.83	3.03	3.56
Ge, 6h (x, y, $^1/_4$)			
x	0.3993(1)	0.3991(3)	0.4004(3)
y	0.3727(1)	0.3725(3)	0.3729(3)
Uiso × 100/Å^2	0.95	2.36	3.08
O(1), 6h (x, y, $^1/_4$)			
x	0.3153(2)	0.3134(5)	0.3181(4)
y	0.4883(2)	0.4867(5)	0.4899(4)
Uiso × 100/Å^2	2.15	4.08	5.17
O(2), 6h (x, y, $^1/_4$)			
x	0.5998(1)	0.6020(4)	0.6018(4)
y	0.4722(1)	0.4705(4)	0.4729(4)
Uiso × 100/Å^2	1.90	3.69	5.23
O(3), 12i (x, y, z)			
x	0.3414(1)	0.3393(4)	0.3395(3)
y	0.2482(1)	0.2476(3)	0.2516(3)
z	0.0629(1)	0.0621(3)	0.0644(3)
Uiso × 100/Å^2	3.51	4.50	5.94
O(4), 2a (0, 0, $^1/_4$)			
Uiso × 100/Å^2	6.18	6.27	7.31

[a] Joint SXRPD and NPD refinement. [b] NPD refinement. [c] The occupation factor for La(2) is 0.90.

NPD patterns have been collected for $La_{9.60}$ and $La_{9.75}$ compositions in order to locate the oxygen positions accurately. The RT joint refinement of the NPD and SXRPD data for $La_{9.60}(GeO_4)_6O_{2.4}$ in s.g. $P6_3/m$ gave an accurate description of the structure. The neutron wavelength was refined in the simultaneous analysis and converged to 1.8856(1) Å. This wavelength was used in all subsequent Rietveld analyses. The final Rietveld disagreement factors and the refined atomic positions for $La_{9.60}$ are given in Table 1. The Rietveld fit of the neutron data is displayed in Figure 2. The anisotropic thermal parameters are given in Table 3 and the bond distances are given in Table 4. It must be stressed that this apatite structure is highly disordered (both in the lanthanum and oxide sublattices). Consequently, the anisotropic thermal refinements gave a much better fit. As an example, R_F for the neutron refinement dropped from 5.7% for the isotropic refinement to 2.8% for the anisotropic fit. This is a very remarkable improvement, and some thermal parameters were huge (Table 3) as their values take into account the static disorder of the structure. The final model has 40 variable atomic parameters (12 being positional and 28 being thermal). The number of reflections was 609 in the SXRPD pattern and 282 in the NPD pattern. The crystallographic formula in Table 1 is $La_{9.60}(GeO_4)_6O_2$ (which is not fully charge-balanced) as the attempts to place the extra oxygen into the channels were unsuccessful.

(37) Rodriguez-Carvajal, J.; Fernandez-Diaz, M. T.; Martinez, J. L. *J. Phys. Condens. Mater.* **1991**, *3*, 3215.
(38) Stephens, P. W. *J. Appl. Crystallogr.* **1999**, *32*, 281.

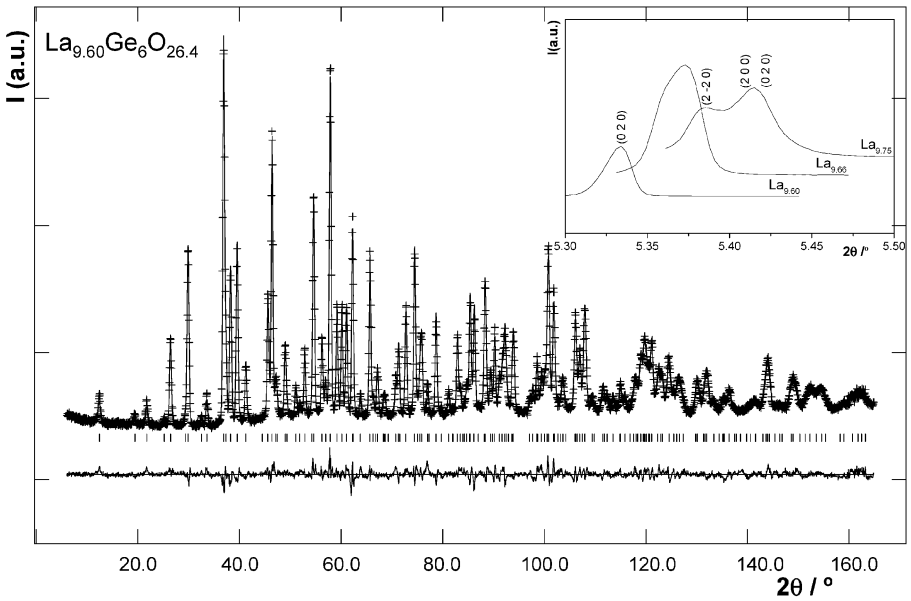

Figure 2. Observed (crosses), calculated (full line), and difference (bottom) RT−NPD patterns for $La_{9.60}(GeO_4)_6O_{2.4}$. The inset shows a selected SXRPD region (5.3−5.5°/2θ) for $La_{9.60}$, $La_{9.66}$, and $La_{9.75}$ compositions showing the triclinic splitting along the series.

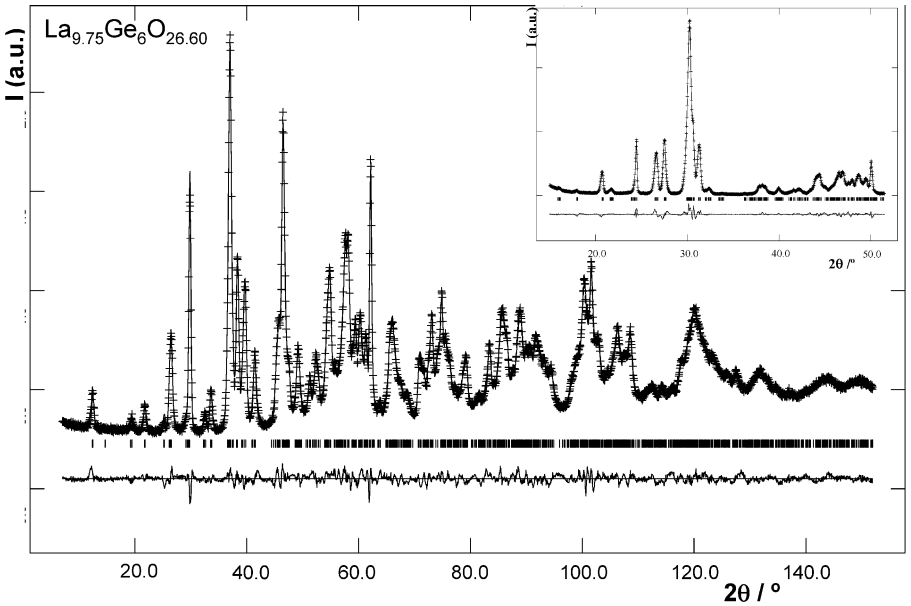

Figure 3. Observed (crosses), calculated (full line), and difference (bottom) NPD pattern for $La_{9.75}(GeO_4)_6O_{2.60}$. The inset shows the fit to the LXRPD pattern.

The joint refinement of SXRPD and NPD data allows the refinement of the germanium occupation factor which converged to full occupancy verifying that there was not germanium loss during the synthesis, in agreement with the results described in the Experimental Section.

It should be underlined that the joint refinement has allowed us to refine the lanthanum occupation factors freely. We have located the vacancies completely ordered at the nine-coordinated La(2) site, in full agreement with previous NPD studies for $La_{9.33}(TO_4)_6O_2$ (T = Si[12], Ge[23]). We have also tested several models for the oxygen disorder inside the apatite channels. However, the models converged to unrealistically short O−O distances. So, we have not placed O(4) out of the special (0 0 $^1/_4$) position. The strong disorder of the oxygen anions along the apatite *c*-axis is clearly seen in the anisotropic thermal parameters, as U_{33} for O(4) is 0.192(4) Å^2 which is extremely high. The anisotropic thermal parameters for $La_{9.33}(GeO_4)_6O_2$ at RT from NPD are also given in Table 3 for the sake of comparison.[23] The strong static disorder, evidenced as very high values of U_{33} for O(4), U_{11} for O(3), and U_{11} and U_{22} for O(1), is fully reproducible.

The RT joint refinement of the NPD and SXRPD data for $La_{9.75}(GeO_4)_6O_{2.62}$ in s.g. $P\bar{1}$ gave a good description of this very complex structure. Both NPD and SXRPD peak shapes were described with the phenomenological multidimensional distribution of lattice metrics approach.[37] The refinement of the thermal vibration factors was isotropic (24 temperature factors) as there are 72 variable positional parameters. On top of that complexity, there is disorder in the structure (due to the atomic nonstoichiometry) which results in the

Table 2. Refined Structural Parameters for $La_{9.75}Ge_6O_{26.62}$ at RT from Joint SXRPD and NPD Refinement[a]

a/Å	9.9368(4)	9.9328(2)		
b/Å	9.9220(3)	9.9309(1)		
c/Å	7.2925(2)	7.2924(1)		
α/°	90.566(3)	90.403(2)		
β/°	88.992(4)	89.304(1)	$R_{wp}{}^S/R_{wp}{}^N$/%	11.71/3.16
γ/°	120.334(3)	120.203(1)	$R_p{}^S/R_p{}^N$/%	8.69/2.46
V/Å^3	620.46(3)	621.64(1)	$R_F{}^S/R_F{}^N$/%	2.64/1.28

	x	*y*	*z*	Uiso × 100/Å^2
La(1a)[b]	0.2178(6)	0.9763(5)	0.2543(7)	−0.6(1)
La(1b)[b]	0.0049(6)	0.2405(6)	0.2529(8)	0.1(1)
La(1c)[b]	0.7518(7)	0.7675(6)	0.2436(7)	0.6(1)
La(2a)[b]	0.3459(9)	0.6509(9)	1.0031(9)	2.0(1)
La(2b)[b]	0.3146(9)	0.6597(8)	0.5021(8)	0.9(1)
Ge(a)	0.4075(7)	0.3874(7)	0.2611(9)	2.3(2)
Ge(b)	0.6294(7)	0.0230(6)	0.2406(9)	1.4(1)
Ge(c)	0.9834(7)	0.6061(7)	0.2558(7)	1.5(2)
O(1a)	0.3258(9)	0.4894(9)	0.2574(11)	1.2(2)
O(1b)	0.5071(9)	0.8224(9)	0.2365(12)	0.8(2)
O(1c)	0.1846(8)	0.7007(7)	0.2277(8)	−0.6(2)
O(2a)	0.6157(9)	0.4679(8)	0.2963(9)	0.1(2)
O(2b)	0.5255(11)	0.1238(9)	0.2402(11)	2.1(2)
O(2c)	0.8615(9)	0.3949(10)	0.2246(10)	1.0(2)
O(3a)	0.3491(10)	0.2716(8)	0.0674(8)	0.2(2)
O(3b)	0.7949(7)	0.0777(7)	0.0676(10)	0.3(2)
O(3c)	0.9024(9)	0.6531(8)	0.0567(8)	−1.3(1)
O(3d)	0.6571(9)	0.7438(9)	0.5656(11)	1.6(2)
O(3e)	0.2632(11)	0.8723(9)	0.5497(11)	3.0(2)
O(3f)	0.0485(9)	0.2783(9)	0.5939(10)	3.4(2)
O(4)	0.0171(12)	0.0021(14)	0.2231(11)	3.7(2)

[a] The unit cell parameters for $La_{9.66}$ from SXRPD data are given in italics. [b] The occupation factor for La is 0.975.

strain-induced peak broadening in the powder patterns (diffraction peaks in the high angle regions are quite broad). Some very small and even negative temperature factors, given in Table 2, are unphysical being caused by the limited quality of the data and the disorder and pseudo-symmetry inherent to this structure. The final Rietveld disagreement factors and the refined atomic positions for $La_{9.75}$ are given in Table 2. The Rietveld fit of the neutron data is displayed in Figure 3 and the inset shows the fit of the triclinic structure to the LXRPD pattern for the sake of comparison. The bond distances are given in Table 5. The crystallographic formula in Table 2 is $La_{9.75}(GeO_4)_6O_2$ (which is not fully charge-balanced) as we could not place the extra oxygen into the channels.

The crystal structure of hexagonal apatite "ideally stoichiometric $La_{10}(GeO_4)_6O_2$" was shown in Figure 1 with the atoms labeled. The lanthanum nonstoichiometry is located at the ($^1/_3$ $^2/_3$ *z*) site (La(2) nine-coordinated) with the (*x y* $^1/_4$) La site (seven-coordinated La(1)) fully occupied. The oxide nonstoichiometry is located at the apatite channels along the [0 0 *z*] direction. The framework for the triclinic distorted apatites ($9.66 \leq 10 - x \leq 9.75$) is the same. However, each lanthanum La(1) splits into three crystallographic independent La atoms La(1a), La(1b), and La(1c); each lanthanum La(2) splits into two La(2a) and La(2b); each tetrahedral GeO_4 group splits into three different units; and O(4) remains unsplit. We have tested ordering of the La-vacancies in the La(2a) and La(2b) sites but the fit does not improve significantly. So, the final reported model (Table 2) has random La-vacancies. However, an indirect insight can be obtained from the coordination polyhedra surrounding the La atom (Table 5). Four lanthanums are eight-coordinated and the remaining one is seven-coordinated. The limit for La−O bond calculations was 3.2 Å. The oxygen environments around the lanthanums are more similar in the triclinic phase which indirectly indicates the disordering of the lanthanum vacancies.

It is important to note that we have prepared $La_{9.75}(SiO_4)_6O_{2.62}$ apatite compound and it does not display

Table 3. Refined Anisotropic Thermal Parameters for $La_{9.60}Ge_6O_{26.4}$ at Different Temperatures[a]

atom	U_{11} × 100	U_{22} × 100	U_{33} × 100	U_{12} × 100	U_{13} × 100	U_{23} × 100
La(1), 6h (*x*, *y*, $^1/_4$)	1.4	0.7	0.8	1.5		
RT	2.0(1)	1.1(1)	0.3(1)	0.7(1)	0	0
773 K	3.2(2)	1.6(1)	2.1(1)	0.7(1)		
1173 K	3.8(1)	2.8(1)	3.0(1)	1.4(1)		
La(2), 4f ($^1/_3$, $^2/_3$, *z*)	2.2	2.2	1.3	1.1		
RT	2.0(1)	2.0(1)	2.0(1)	1.0(1)	0	0
773 K	3.5(1)	3.5(1)	2.3(2)	1.8(1)		
1173 K	4.4(1)	4.4(1)	3.8(2)	2.2(1)		
Ge, 6h (*x*, *y*, $^1/_4$)	1.1	0.4	0.9	0.5		
RT	1.6(1)	0.6(1)	1.2(1)	1.2(1)	0	0
773 K	2.6(1)	2.2(1)	2.7(1)	1.7(1)		
1173 K	2.9(1)	2.8(1)	3.5(1)	1.5(1)		
O(1), 6h (*x*, *y*, $^1/_4$)	4.5	4.2	2.1	4.2		
RT	6.6(1)	5.7(1)	1.3(1)	6.0(1)	0	0
773 K	8.5(4)	6.2(3)	2.0(2)	5.2(3)		
1173 K	9.3(3)	7.1(3)	4.5(2)	6.2(3)		
O(2), 6h (*x*, *y*, $^1/_4$)	1.5	0.3	4.4	0.2		
RT	0.6(1)	0.1(1)	4.5(1)	0.3(1)	0	0
773 K	3.7(2)	2.7(2)	4.7(3)	1.7(2)		
1173 K	3.8(2)	2.7(2)	9.2(4)	0.9(2)		
O(3), 12i (*x*, *y*, *z*)	9.3	2.7	0.9	3.4	−2.9	−0.9
RT	12.1(1)	3.0(1)	2.5(1)	4.9(1)	−3.6(1)	−1.9(1)
773 K	12.9(3)	3.8(2)	3.4(2)	5.3(2)	−4.4(2)	−2.1(1)
1173 K	14.8(3)	4.7(2)	5.2(2)	5.7(2)	−4.8(2)	−2.3(1)
O(4), 2a (0, 0, $^1/_4$)	0.7	0.7	13.1	0.3		
RT	0.3(1)	0.3(1)	19.2(4)	0.1(1)	0	0
773 K	3.1(3)	3.1(3)	17.6(9)	1.5(1)		
1173 K	3.9(6)	3.9(3)	17.3(8)	1.9(1)		

[a] The anisotropic thermal parameters for $La_{9.33}Ge_6O_{26}$ at RT from ref 23 are given in italics. The RT refinement was carried out with SXRPD and NPD data. The HT refinements were carried out with only NPD data.

Table 4. Selected Bond Distances (Å) for $La_{9.60}Ge_6O_{26.4}$ at Different Temperatures

	RT[a]	773 K[b]	1173 K[b]
La(1)−O(1)	2.782(2)	2.763(6)	2.839(5)
La(1)−O(2)	2.537(1)	2.594(4)	2.587(4)
La(1)−O(3) × 2	2.616(1)	2.639(4)	2.654(4)
La(1)−O(3) × 2	2.454(1)	2.451(2)	2.480(2)
La(1)−O(4)	2.369(1)	2.346(2)	2.342(2)
⟨La(1)−O⟩	2.55	2.56	2.58
La(2)−O(1) × 3	2.486(2)	2.482(4)	2.493(4)
La(2)−O(2) × 3	2.563(2)	2.565(4)	2.582(4)
La(2)−O(3) × 3	2.940(1)	2.968(3)	2.990(3)
⟨La(2)−O⟩	2.66	2.67	2.69
Ge−O(1)	1.728(1)	1.731(4)	1.736(4)
Ge−O(2)	1.725(1)	1.751(4)	1.746(3)
Ge−O(3) × 2	1.732(1)	1.746(3)	1.720(2)
⟨Ge−O⟩	1.729	1.744	1.731

[a] Joint SXRPD and NPD refinement. [b] NPD refinement.

the triclinic distortion. This difference cannot be solely ascribed to the oxygens in the channels but also to the larger flexibility of the GeO_4 tetrahedra when compared to the SiO_4 groups. In fact, the average Ge−O distances are different for the three tetrahedra (Table 5), with the mean Ge(a)−O distance being shorter than those of Ge(b) and Ge(c). The results for the Si-based apatite series will be reported elsewhere.

With the clarified picture in the La_2O_3−GeO_2 apatite phase diagram domain, it is possible to explain previously controversial results. Figure 2 of ref 20 showed the powder patterns of a sample with nominal stoichiometry $La_{9.33}(GeO_4)_6O_2$ heated at 1423, 1623, and 1773 K. The pattern at 1423 K is typical of the hexagonal structure and the patterns at 1623 K (20 h) and 1773 K (6 h) are typical of the triclinic structure (inset of Figure 3). The change in the patterns is due to the Ge loss, which increases the La/Ge ratio in the apatite phase, resulting in a hexagonal-to-triclinic conversion. On the other hand, the reports from the Ishihara's group[30] claiming that the high-temperature phases for La/Ge ratios close to 1.60:1 have a $La_{2-x}GeO_5$ type structure are not supported in our study. The compounds have patterns fully compatible with the triclinic apatite structure reported here (see inset of Figure 3).

High-Temperature Crystal Structures. We have carried out a high-temperature NPD study for $La_{9.60}$ because we detected two conduction regimes in the impedance study, vide infra. High-temperature data were collected at 1173 K (regime **I**) and 773 K (regime **II**). We cannot detect a symmetry change on heating and both patterns were analyzed in the s.g. $P6_3/m$. The results of the refinements of the NPD data are given in Table 1. The anisotropic thermal parameters are given in Table 3 and the bond distances are given in Table 4.

The analysis of the high-temperature atomic parameters for $La_{9.60}$ rules out a structural transition on heating. The bond distances slightly increase due to the thermal expansion and the thermal parameters increase on heating as expected. Based on these three reported unit cell volumes, we can estimate the volume thermal expansion coefficient value for $La_{9.60}$, as $\alpha_v = 8 \cdot 10^{-6}\ K^{-1}$ [where α_v is defined as $m/3n$ for $V(T) = n + mT(K)$ under the approximation of a linear evolution which was confirmed with a thermodiffractometric LXRPD study although having slightly larger errors]. We have done a similar study for $La_{9.75}$ with thermodiffractometric LXRPD data. The data analysis is complex due to the strong overlapping in the pattern. We have estimated α_v as $5 \cdot 10^{-6} K^{-1}$ for $La_{9.75}$ and we can confirm that there is no phase transition on heating to 1273 K. These results are in agreement with the DTA study in the sense that it also did not show any phase transition on heating below 1473 K for any of the compositions.

Impedance Study. Representative impedance data for one composition, $La_{9.60}$, at two temperatures are shown as impedance complex plane plots in Figure 4; similar plots were obtained for all compositions. Data show a single, slightly depressed, arc at high frequencies/low temperatures. With increasing temperature, lower frequency effects are seen, in the form of an inclined spike (see inset) at an angle tilted ∼45° to the Z′ axis. The associated capacitance for the low frequency point in the spike was close to 0.22 μF. Such a spike is characteristic for the diffusion-limited process represented by a Warburg impedance; in the present case, the origin is likely to be the diffusion of oxygen toward/away from the electrode/sample contact. In fact, when moving from dominant ionic to mixed conduction and dominant electronic conduction, the low-frequency response tends to vanish as a consequence of a decreasing relevance of the low relaxation frequency processes

Table 5. Selected Bond Distances (Å) for $La_{9.75}Ge_6O_{26.625}$ at RT from Joint SXRPD and NPD Refinement

La(1a)−O(1c)	2.590(8)	La(1b)−O(1a)	2.884(10)	La(1c)−O(1b)	2.749(10)
La(1a)−O(2b)	2.640(10)	La(1b)−O(2c)	2.577(10)	La(1c)−O(2a)	2.599(8)
La(1a)−O(3a)	2.880(9)	La(1b)−O(3b)	2.332(8)	La(1c)−O(3a)	2.443(10)
La(1a)−O(3b)	2.394(8)	La(1b)−O(3c)	2.460(9)	La(1c)−O(3b)	3.167(9)
La(1a)−O(3d)	2.734(9)	La(1b)−O(3e)	2.703(10)	La(1c)−O(3c)	2.646(10)
La(1a)−O(3e)	2.542(11)	La(1b)−O(3f)	2.523(9)	La(1c)−O(3d)	2.483(9)
La(1a)−O(3f)	2.795(10)	La(1b)−O(4)	2.436(11)	La(1c)−O(3f)	2.560(11)
La(1a)−O(4)	2.151(10)			La(1c)−O(4)	2.487(13)
La(2a)−O(1a)	2.402(11)	La(2b)−O(1a)	2.485(11)		
La(2a)−O(1b)	2.375(10)	La(2b)−O(1b)	2.612(11)		
La(2a)−O(1c)	2.487(11)	La(2b)−O(1c)	2.545(8)		
La(2a)−O(2a)	2.584(9)	La(2b)−O(2a)	2.281(10)		
La(2a)−O(2b)	2.625(11)	La(2b)−O(2b)	2.693(11)		
La(2a)−O(2c)	2.524(10)	La(2b)−O(2c)	2.504(11)		
La(2a)−O(3a)	2.764(11)	La(2b)−O(3d)	3.110(11)		
La(2a)−O(3c)	2.806(10)	La(2b)−O(3e)	2.429(10)		
Ge(a)−O(1a)	1.585(10)	Ge(b)−O(1b)	1.779(9)	Ge(c)−O(1c)	1.736(9)
Ge(a)−O(2a)	1.825(11)	Ge(b)−O(2b)	1.712(10)	Ge(c)−O(2c)	1.829(10)
Ge(a)−O(3a)	1.725(10)	Ge(b)−O(3b)	1.916(8)	Ge(c)−O(3c)	1.845(8)
Ge(a)−O(3d)	1.692(9)	Ge(b)−O(3e)	1.846(11)	Ge(c)−O(3f)	1.717(10)
⟨Ge(a)−O⟩	1.707	⟨Ge(b)−O⟩	1.813	⟨Ge(c)−O⟩	1.782

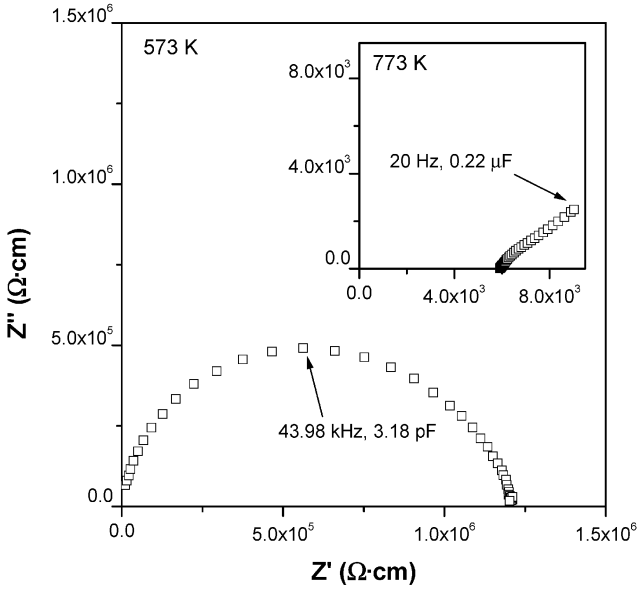

Figure 4. Complex impedance plane plot for $La_{9.60}(GeO_4)_6O_{2.4}$ at 573 K (773 K in the inset).

involved in the electrode reaction. This suggests that ionic transport is indeed playing a main role in these materials. To confirm this, complementary electrochemical measurements of conductivity versus oxygen partial pressure were also performed and the study is described below.

Figure 5 shows modulus data at different temperatures for the same sample, $La_{9.60}$, on a double-logarithmic scale. Well-defined maxima can be observed with clear power law behavior at both sides of the peak. To investigate the electrical microstructure of the pellets, and in particular to determine whether the overall pellet resistances represented the bulk resistance of the grains or whether they were influenced by grain boundary effects, the experimental data were replotted as the imaginary parts of the impedance, Z″, and as electric modulus, M″, against log(frequency) (inset in Figure 5). The maxima of both curves are very close (they are separated by less than a half decade in frequency) which indicates that the impedance peak is associated with the same RC element responsible for the modulus peak. The associated capacitances (1.9 pF for M″ and 2.1 pF for Z″) are characteristic for the bulk response. Hence, the semicircle of the Nyquist plot in Figure 4 corresponds to the bulk contribution and the intersection at low frequency with Z′ axis is the bulk impedance, apparently free from grain boundary contributions.

Bulk conductivities as functions of temperature are shown in the form of an Arrhenius plot in Figure 6. The results for the four single-phase samples are displayed. A plot of $\mathrm{Ln}(\sigma T)$ vs $1000/T$ should give a straight line of slope $-E_a/k$ if the activation energy E_a was independent of temperature. However, two regimes with quite different activation energies can be observed. Below 973 K (low-temperature regime labeled **II**), the Arrhenius plots for the bulk conductivities fall on a set of approximately parallel lines, showing a maximum in conductivity for $La_{9.60}$. The conductivity values for these four compositions are very close and the maximum difference is lower than half an order of magnitude. The activation energies are given in the inset of Figure 6 and range between 0.99 and 1.23 eV. Above 973 K (high-temperature regime labeled **I**), the Arrhenius plots for

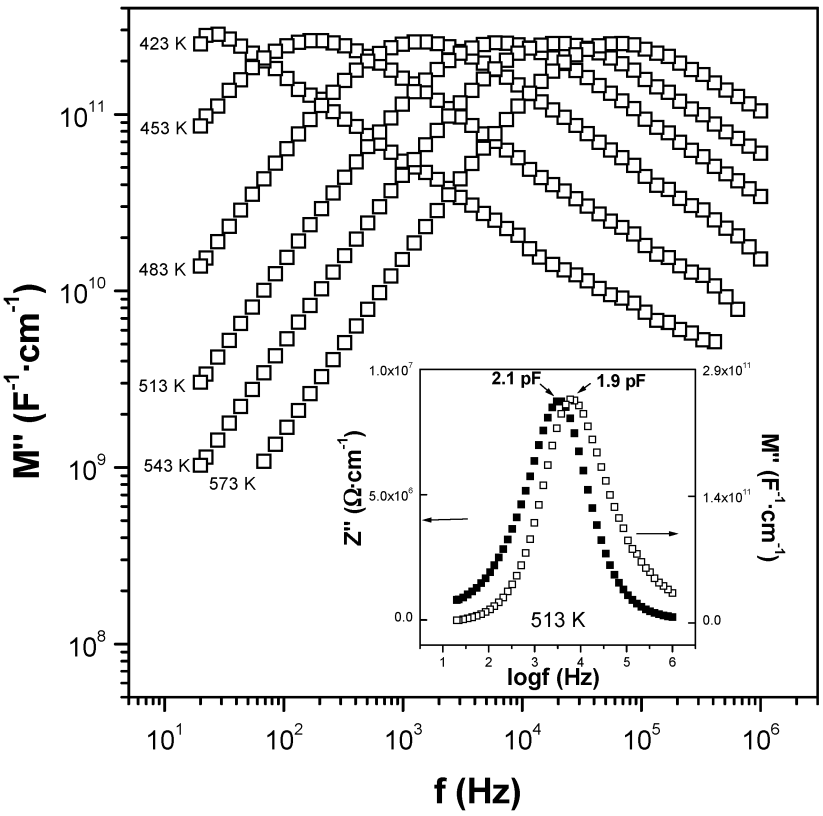

Figure 5. Imaginary part of the modulus vs frequency at several selected temperatures for $La_{9.60}(GeO_4)_6O_{2.4}$. The inset shows the spectroscopic plots of Z″ and M″ vs logf at 513 K for the same composition.

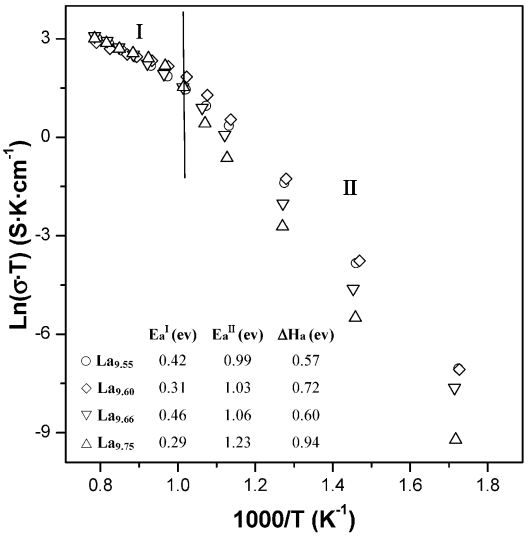

Figure 6. Variation of $\log(\sigma_{bulk}T)$ versus $1000/T$ for $La_{9.55}$, $La_{9.60}$, $La_{9.66}$, and $La_{9.75}$ compositions. The table in the inset shows the activation energies (eV) in the two regimes: **I** at high temperatures (above 973 K), and **II** at low temperatures (below 973 K). The association enthalpy (ΔH_a/eV) values are also given (see text for details).

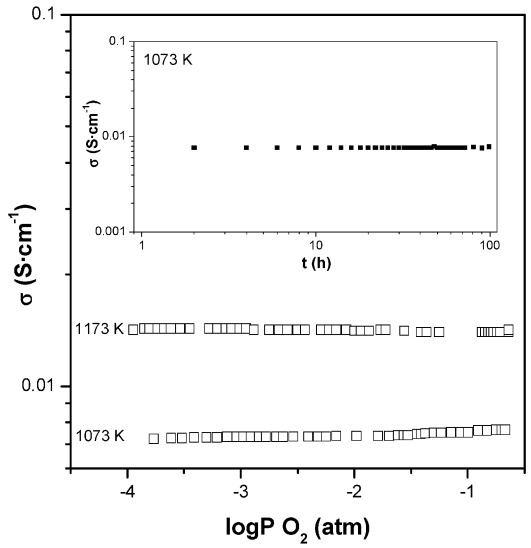

Figure 7. Total conductivity at 1073 and 1173 K as a function of oxygen partial pressure (atm) for $La_{9.55}$. The inset shows the evolution of conductivity with time in air at 1073 K.

the bulk conductivities coincide and the activation energies are much smaller, ranging between 0.29 and 0.42 eV. We note that the differences in compositions for the four single phases in the system are not very large and are lying between $La_{9.55}(GeO_4)_6O_{2.32}$ and $La_{9.75}(GeO_4)_6O_{2.62}$.

From these plots, we have determined the bulk conductivities at 873 K which were $1.6 \cdot 10^{-3}$, $2.0 \cdot 10^{-3}$, $1.2 \cdot 10^{-3}$, and $0.6 \cdot 10^{-3}$ S·cm^{-1} for $La_{9.55}$, $La_{9.60}$, $La_{9.66}$, and $La_{9.75}$ samples, respectively. The values coalesce to $7.0 \cdot 10^{-3}$ S·cm^{-1} at 1073 K. The conductivities are similar to the value reported for a compound with the nominal stoichiometry "$La_{9.33}(GeO_4)_6O_2$" being $2.9 \cdot 10^{-3}$ S·cm^{-1} at 873 K.[22] The conductivites of the germanium apatites are higher than those of the silicon apatites. For instance, the value of $0.3 \cdot 10^{-3}$ S·cm^{-1} at 873 K was reported for $La_{9.33}(SiO_4)_6O_2$.[11]

A remarkable curvature may be observed in the Arrhenius plot close to 973 K (see Figure 6), which is a known behavior for some oxide-ion conductors. This change in the activation energies is not due to a phase transition as demonstrated in the high-temperature NPD study. The bulk activation energy (E_a) is usually the sum of the migration enthalpy (ΔH_m) and the association enthalpy (ΔH_a) terms. At low temperatures (regime **II**), both are present, but with increasing temperature the Coulomb forces between positive (oxygen vacancies) and negative defects (lanthanum vacancies) decrease due to increased thermal energy, leaving only ΔH_m at elevated temperatures (regime **I**). The change in slope between the low and the high-temperature intervals provides an estimate for the association enthalpy. The two straight lines in the curved Arrhenius plots were determined by fitting to a regression coefficient better than 0.995. Migration enthalpies and ionic conductivities in regimes **I** and **II** are shown in Figure 6. The association enthalpies are about 0.7 eV for this series and are larger than those reported for oxide conductors with fluorite or perovskite-type structures.[39,40] Alternative explanations for these changes in slope include the following: (i) an enhanced role of grain boundaries at low temperature (usually resulting in higher activation energies); (ii) changes in the dominant charge carriers from ionic to electronic with increasing temperature; or (iii) changes in the dominant charge carriers with nonnegligible lanthanum contribution to the ionic conductivity at high temperatures. Although there is not yet experimental evidence to support any of these alternative explanations, the scatter in high- and low-temperature activation energies and corresponding association enthalpies seems excessive for similar materials with presumably similar transport mechanisms. Additional experimental evidence is thus required to provide definitive support to any of the previously mentioned explanations.

It is well-known that the total conductivity for *n*-type semiconductors increases as the oxygen partial pressure decreases, and conversely, the conductivity for *p*-type semiconductors decreases. On the other hand, the total conductivity is independent of the oxygen partial pressure when the ionic conductivity is dominant. The conductivity data for one composition, $La_{9.55}$, at 1073 and 1173 K as a function of oxygen partial pressure are shown in Figure 7. Similar plots were obtained for the three remaining compositions. As it can be seen, the conductivity is almost independent of oxygen partial pressure, which suggests pure oxide-ion conduction with negligible electronic contribution within this limited oxygen partial pressure range.

The stability of $La_{10-x}(GeO_4)_6O_{3-1.5x}$ apatite phases has been characterized under different conditions. First, the conductivity of $La_{9.55}$ was measured at 1073 K in air up to 1 week, as shown in the inset of Figure 7. The oxide ion conductivity is stable at 1073 K because the phase does not undergo degradation. This is in agreement with the results from the 1173 K NPD study which lasted 10 h in air. Second, the conductivities under

(39) Huang, K.; Tichy, R. S.; Goodenough, J. B. *J. Am. Ceram. Soc.* **1998**, *81*, 2565.
(40) Kilner, J. A.; Brook, R. J. *Solid State Ionics* **1982**, *6*, 237.

reducing conditions, obtained in a N_2-H_2 atmosphere (P_{O_2} ranged from air to around 10^{-21} atm), were tested at 1073 K but they are not shown. During the measurement acquisition times, some anomalies were detected. Ex-situ powder diffraction studies of the treated pellets revealed the presence of new phases, for instance Pt_3Ge and $La(OH)_3$ (PDF nos. 15-0590 and 75-1900, respectively). Hence, reduction of the apatite compounds, catalyzed by the Pt electrodes, has taken place. Third, $La_{10-x}(GeO_4)_6O_{3-1.5x}$ apatite pellets also undergo slight decomposition when stored in a can under dried air for several months. Minor amounts of $La(OH)_3$ were detected in the stored pellets (identified by LXRPD data) which caused drastic decrease of the conductivities.

Conclusions

We have synthesized single-phase apatite compounds in a narrow compositional range between $La_{9.55}(GeO_4)_6O_{2.32}$ and $La_{9.75}(GeO_4)_6O_{2.62}$. The phases are hexagonal for lanthanum contents lower than $La_{9.60}$ and triclinic for the higher lanthanum contents. The triclinic apatite structure is very complex but the joint refinement of NPD and SXRPD data has allowed us to obtain a good description of the crystal structure which contains 24 crystallographically independent atoms. The high-temperature NPD study for hexagonal $La_{9.60}(GeO_4)_6O_{2.40}$ has shown that there is no phase transition up to 1173 K. The samples are oxide ion bulk conductors and the curvature in the Arrhenius plots allowed determination of the migration and association enthalpies. The stability of these conductors has also been characterized with promising results for tests slightly in excess of 100 hours.

Acknowledgment. The work in Málaga has been supported by the MAT2000-1585-C3-3 research grant. L.L.R. thanks the Junta de Andalucía for a studentship. We thank Dr. V. Kharton and Mr. A. Shaula (Aveiro) for their assistance with the electrical characterization. ESRF is thanked for the provision of X-ray synchrotron facilities. This work was partially performed at the spallation neutron source SINQ, Paul Scherrer Institut, Villigen, Switzerland.

CM031017U